ACADEMIC PRESS

Available online at www.sciencedirect.com

SCIENCE DIRECT®

Journal of Sound and Vibration 269 (2004) 933–963

JOURNAL OF SOUND AND VIBRATION

www.elsevier.com/locate/jsvi

Detailed ball bearing model for magnetic suspension auxiliary service

G. Sun[a,*], A.B. Palazzolo[a], Andrew Provenza[b], Gerald Montague[c]

[a] *Department of Mechanical Engineering, Texas A&M University, 100 Engineering/Physics Building, College Station, TX 77843-3123, USA*

[b] *NASA Glenn, Cleveland, OH, USA*

[c] *US Army at NASA Glenn, Cleveland, OH, USA*

Received 7 January 2002; accepted 15 January 2003

Abstract

Catcher bearings (CBs) provide backup protection for rotating machines with active magnetic bearings (AMBs). The CBs are required in the event of an AMB failure or high transient loads. Numerical simulations of a rotor drop on CBs in flywheel energy storage system are conducted with a detailed CB model which includes a Hertzian load–deflection relationship between mechanical contacts, speed-and-preload-dependent bearing stiffness due to centrifugal force, and a Palmgren's drag friction torque. The transient simulation results show the rotor shaft response variations with the design parameters: shaft/bearing friction coefficients, axial preload, support damping of damper liner, and side loads from magnetic bearings. The results reveal that friction coefficients, support damping, and side loads are critical parameters to satisfy CB design objectives and prevent backward (super) whirl.

1. Introduction

Active magnetic bearings (AMBs) have been increasingly used in many rotor dynamic applications because they have several advantages over conventional bearings: no lubrication required, no mechanical friction loss, and adjustable bearing characteristics such as stiffness and damping. In an AMB system, the rolling-element CBs are necessary to protect the MB, stator, and stationary components along the shaft.

*Corresponding author.
E-mail address: sungy@tamu.edu (G. Sun).

0022-460X/03/$ - see front matter
doi:10.1016/S0022-460X(03)00207-4

The paper of Gelin et al. [1] included numerical simulation and landing tests of an industrial centrifugal compressor with a Coulomb friction contact force ignored in the numerical model. Ishii and Kirk [2] presented the numerical results of the transient response of a flexible rotor drop, which showed an optimum damping can be chosen to prevent destructive backward whirl; however, the rotor model they used did not include gyroscopic effects. They [3] later refined the initial analysis [2] and included features that more closely match the conditions during an actual rotor drop. Fumagalli et al. [4] classified the touchdown process into four distinct phases of motion—free fall, impact, sliding, and rolling—and investigated the influences of such parameters as air gap, friction coefficient, and damping on the impact dynamics. Foiles and Allaire [5] also numerically analyzed the effects of parameters for non-linear models on two types of rotors: generator or turbine rotor and centrifugal compressor rotor. Their work did not include the effects of support damping and stiffness.

Kirk et al. [6] performed experimental rotor drop tests for balanced and unbalanced conditions. The authors concluded that a major influence on the transient response is the balance level of the rotor. In Part II [7], a finite element code for the rotor and bearing system was developed to perform stability analysis and unbalance response. They compared the analytical and experimental results for the damped critical speeds and unbalance response. Swanson et al. [8] showed the test results for 5 CB configurations in which 38 drops with varying rotor speed, unbalance amplitude and location were performed. Tessier [9] described the development, testing, and delevitation tests of a flexible compressor rotor which is 2 m in length and 360 kg in weight. The zero clearance auxiliary bearing (ZCAB) was introduced by Chen et al. [10]. The tests verified that the possibility of a backward whirl of a rotor can be reduced due to clearance elimination and the ZCAB damping.

In Ref. [11], steady state behavior was numerically investigated and analyzed for various parametric configurations: rotor imbalance, support stiffness and damping. Ecker [12] presented the steady state numerical results for a rigid rotor with imbalance rotor on a CB fixed to the bearing housing. The most important point of steady state behavior is whether or not a rotor enters into a full whirl in the CB clearance. Feeny [13] explored the stability of cylindrical and conical whirls in a perfectly balanced and rigid rotor on rigid retainer bearings. Maslen and Barrett [14] derived whirl conditions of a circularly isotropic rotor and CB support along with the test results of a commercial compressor rotor with CBs.

The inner race speed and axial preload-dependent bearing stiffness is an important issue in high-speed bearing modelling because bearing stiffness is determined according to these two parameters. Most papers on the numerical analysis of CBs have utilized simple simulation models, while non-CB papers utilize more sophisticated ball bearing models. For instance, a rolling element bearing stiffness matrix depending on axial preload and inner race speed was calculated analytically, using an iterative Newton–Raphson procedure in Ref. [15] for non-CB applications. Similarly, Shin [16] showed that axial and radial stiffness decreases substantially as inner race spinning speed increases. He later developed a bearing model including thermal expansion of bearing components in Ref. [17]. These two authors used different approaches but obtained similar results of speed-dependent radial and axial stiffness of a bearing.

In this paper, a detailed CB model is developed based on the same method as Ref. [15] including centrifugal force on balls, Hertzian contact load–deflection relationship, inner race speed-and-axial preload-dependent stiffness, and power loss due to friction force on inner race and

Palmgren's drag torque. The CB model provides an accurate bearing stiffness accounting for axial preload and inner race speed. A variety of parametric studies such as axial preloads, friction coefficients, support dampings, and side loads from MBs have been performed. The numerical results are compared using 15 performance indices to identify improved CB design features.

2. Rotor drop simulation model

A rigid vertical rotor shaft with a rigid motor and a flywheel connected to it by flexible hubs is depicted in Fig. 1. The hubs are assumed to be torsionally rigid. The integrated shaft is modelled with 16 degrees of freedom (d.o.f.) including cross-coupled stiffness and gyroscopic moments. The shaft has three translational and three rotational motions, while the flywheel and motor have three translational and two rotational motions, each. The flywheel and motor generate unbalance forces with 90° phase difference, and the rotor is assumed to be well balanced. Fig. 2 shows a bottom view of the top CB, which is modelled as a 5 d.o.f. system. The inner and outer races each have two transverse motions in the radial direction and the inner race has one spin motion. The bottom CB is modelled as a 7 d.o.f. system. The inner and outer races have two translational motions in the radial direction and one axial motion, and the inner race has one spin motion. Fig. 3 shows the axial rotor drop model. The CBs are modelled as back-to-back duplex pairs at each end. Duplex bearings are matched pairs of bearings with built-in means of preloading. The inner or outer ring faces of these bearings have been selectively relieved a precise amount called the preload offset. Duplexing is used to greatly increase radial and axial rigidity. Duplex bearings

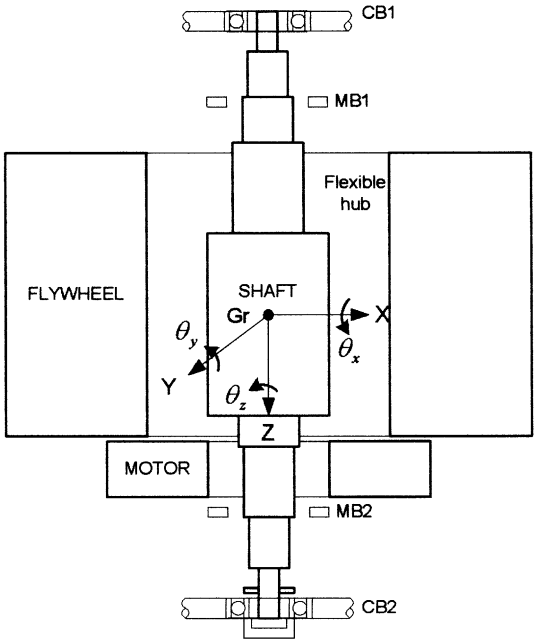

Fig. 1. Energy storage flywheel supported on MBs and CBs.

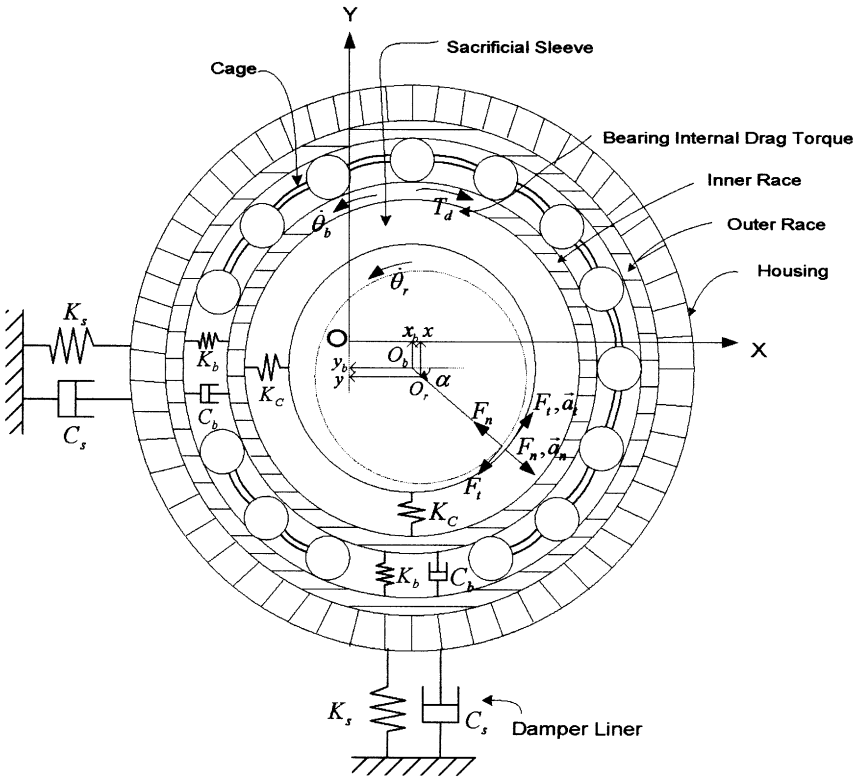

Fig. 2. Detailed catcher bearing model.

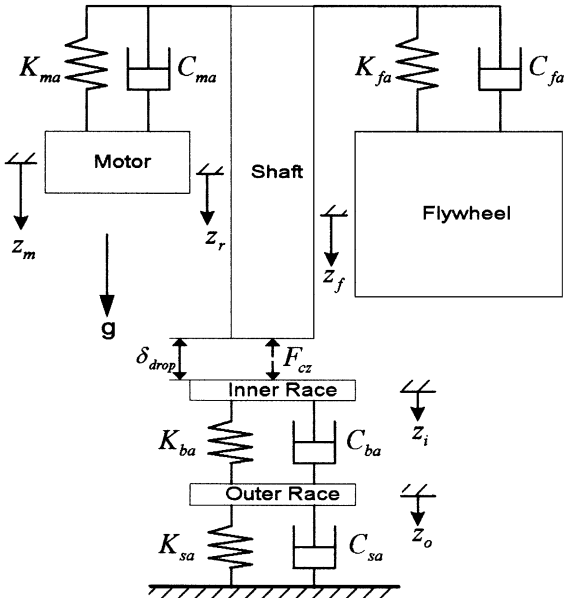

Fig. 3. Axial catcher bearing model.

can withstand bidirectional loads (DB: back to back and DT: face to face mounting) or heavy unidirectional loads (DT mounting). Other advantages include easy assembly and minimum runout. The frame of reference (O, X, Y) is fixed to the machinery frame. The geometric centers of the rotor and bearing inner race are O_r and O_b, respectively. (x, y) is the location of O_r in the frame of reference while (x_b, y_b) is the location of O_b in the frame of reference. The stiffness K_c represents the non-linear Hertzian contact forces [18] between the rotor and inner race, and K_b denotes the stiffness which depends on inner race speed and preload in Ref. [16].

The terms K_s and C_s are the stiffness and damping coefficients of the damper liner. The same duplex pairs CBs are modelled at the top and bottom. Normal (F_n) and tangential $(F_t$, friction) contact forces exist between the spinning rotor and inner race. In the simulation scenario, the shaft drops onto the bottom CB by gravity, simultaneously moving to the CBs in X and Y directions. The rotational speed of the bottom CB inner race is accelerated by the axial and radial contacts with the shaft, while the shaft speed is decelerated by the contacts. The terms (K_{ma}, C_{ma}) and (K_{fa}, C_{fa}) are axial stiffness and damping coefficients of the hubs for the motor and flywheel, respectively. The term F_{cz} is the normal contact force from the axial drop of the shaft onto the inner race of the bottom CB and δ_{drop} is the initial drop height. The stiffness and damping coefficients between inner and outer races are represented as K_{ba} and C_{ba}. The terms K_{sa} and C_{sa} are the stiffness and damping coefficient of the axial support system.

From Fig. 2, the angle at the contact between the rotor and CB is

$$\alpha_j = \tan^{-1}\left(\frac{y_j - y_{bj}}{x_j - x_{bj}}\right), \quad j = 1, 2, \tag{1}$$

where subscripts 1, 2 represent the top and bottom bearings, respectively.

When the rotor shaft hits the CB, a non-linear normal contact force F_n occurs and is given by Hertzian theory [18] as

$$F_{nj} = \begin{cases} Ks_j^n, & s_j \geq 0, \\ 0, & s_j < 0, \end{cases} (j = 1, 2), \tag{2}$$

where $s_j = \sqrt{(x_j - x_{bj})^2 + (y_j - y_{bj})^2} - c$ and the constant K depends on both the material property and contact geometry, c is the radial clearance between the shaft and the CB, and n is dependent on the type of contact: $n = 10/9$ for line contact and $3/2$ for point contact. The friction force is

$$F_{tj} = \mu_d F_{nj}, \quad j = 1, 2, \tag{3}$$

as long as slipping exists at the contact point, where μ_d is the dynamic friction coefficient.

A rolling condition is applied to the model when the tangential velocity of the inner race reaches that of the shaft at the contact point. The rotational equations of motion (EOM) for the rotor, and the inner races of the top and bottom CBs are

$$I_p \ddot{\theta}_r = -(F_{t1} + F_{t2})R_r - T_{za}, \tag{4}$$

$$I_{pb} \ddot{\theta}_{i1} = F_{t1} R_b - T_{d1}, \tag{5}$$

$$I_{pb} \ddot{\theta}_{i2} = F_{t2} R_b - T_{d2} + T_{za}, \tag{6}$$

where T_{za} is the driving torque from axial contact between the shaft and bottom CB, $T_{dj} (j = 1, 2)$ is the drag torque, R_r and R_b denote the radii of the rotor shaft and inner race, and I_p and I_{pb}

denote the polar moments of inertia of the total flywheel system and inner race, respectively. These inertias are referenced to their mass centers. Three possible rolling conditions are considered:

(1) Only the top CB satisfies the rolling condition:

$$R_r\dot{\theta}_r = R_b\dot{\theta}_{i1}. \tag{7}$$

By arranging Eqs. (4) and (5) and using the rolling condition (7), the friction force at the top CB becomes

$$F_{t1} = \frac{R_b/I_{pb}\cdot T_{d1} - R_r/I_p\cdot(F_{t2}R_r + T_{za})}{R_r^2/I_p + R_b^2/I_{pb}}, \text{ where } F_{t2} = \mu_d F_{n2}. \tag{8}$$

(2) Only the bottom CB satisfies the rolling condition:

$$R_r\dot{\theta}_r = R_b\dot{\theta}_{i2}. \tag{9}$$

By arranging Eqs. (4) and (6) and using the rolling condition (9), the friction force at the bottom CB becomes

$$F_{t2} = \frac{R_b/I_{pb}\cdot(T_{d2} - T_{za}) - R_r/I_p\cdot(F_{t2}R_r + T_{za})}{R_r^2/I_p + R_b^2/I_{pb}}, \text{ where } F_{t1} = \mu_d F_{n1}. \tag{10}$$

(c) Both CBs simultaneously satisfy the rolling condition:

$$R_r\dot{\theta}_r = R_b\dot{\theta}_{i2} = R_b\dot{\theta}_{i1}. \tag{11}$$

By arranging Eqs. (4)–(6), and using the rolling condition (11), the friction forces become

$$\begin{Bmatrix} F_{t1} \\ F_{t2} \end{Bmatrix} = \begin{bmatrix} \dfrac{R_r^2}{I_p} + \dfrac{R_b^2}{I_{pb}} & \dfrac{R_r^2}{I_p} \\ \dfrac{R_r^2}{I_p} & \dfrac{R_r^2}{I_p} + \dfrac{R_b^2}{I_{pb}} \end{bmatrix}^{-1} \left\{ \frac{R_b}{I_{pb}} \begin{bmatrix} T_{d1} \\ T_{d2} \end{bmatrix} - T_{za} \begin{bmatrix} \dfrac{R_r}{I_p} \\ \dfrac{R_r}{I_p} + \dfrac{R_b}{I_{pb}} \end{bmatrix} \right\}. \tag{12}$$

Termination or continuation of rolling contact is determined by Eqs. (8), (10) and (12), i.e.,

(a) If $F_{tj} > \mu_s F_{nj}$, then the shaft slides again, i.e., $F_{tj} = \mu_d F_{nj}$, $j = 1, 2$.
(b) If $F_{tj} < \mu_s F_{nj}$, then the shaft keeps rolling on the CB.

The axial normal contact force F_{cz} is determined from $F_{cz} = K_c\Delta$ for $\Delta > 0$, $F_{cz} = 0$ for $\Delta < 0$, where K_c is the contact stiffness from Timoshenko [19] and equals

$$K_c = E\sqrt{\pi(r_2^2 - r_1^2)}/0.96(1 - \nu^2),$$

where $\Delta = (z_r - z_i) - \delta_{drop}$ is the axial contact deflection between the CB inner race and the shaft. The parameter r_1 is the bore radius and r_2 is the relieved face radius of the CB. The torque T_{za} is derived from

$$T_{za} = \int r\,\mathrm{d}F_t,$$

where $F_t = \mu_d F_{cz} = \mu_d P_{cz}\ A$ and A is the axial contact area on the CB. F_{cz} is the axial normal contact force and μ_d is the coefficient of friction.

$$T_{za} = \int_{r1}^{r2}\int_0^{2\pi} r(\mu_d P_{cz} r\,\mathrm{d}\theta\,\mathrm{d}r) = \int_{r_1}^{r_2}\int_0^{2\pi} r^2\mu_d F_{cz}/A\,\mathrm{d}\theta\,\mathrm{d}r$$
$$= \frac{2\pi\mu_d}{A}F_{cz}\frac{(r_2^3 - r_1^3)}{3}.$$

Since $A = \pi(r_2^2 - r_1^2)$,

$$T_{za} = \frac{2\mu_d(r_2^3 - r_1^3)}{3(r_2^2 - r_1^2)}F_{cz}. \tag{13}$$

The friction torque acting on the CB is composed of two parts. The first part T_{dl} is due to applied loads and the second part T_{dv} is the viscous friction torque, which is independent of loads and depends primarily on the characteristics and quantity of lubricant in the bearings.

The first type of torque is determined from an empirical evaluation by Palmgren, as cited in Ref. [18]:

$$T_{dl} = f_1 F_\beta d_m, \tag{14}$$

where f_1 is a factor depending on bearing design and relative bearing load, and d_m is the pitch diameter of the bearing. The force F_β depends on the magnitude and direction of the applied loads. For rolling element bearings, f_1 varies from 0.0001 to 0.00055.

Palmgren also developed a formula for the second type of friction torque:

$$T_{dv} = 10^{-7} f_o (v_o n)^{2/3} d_m^3 \text{ for } v_o n > 2000, \tag{15}$$

$$T_{dv} = 160 \times 10^{-7} f_o d_m^3 \text{ for } v_o n \leqslant 2000, \tag{16}$$

where f_o is a factor depending on the type of bearing and the method of lubrication. For grease packed ball bearings (normally used in CBs) this factor ranges from 1.5 to 5. The parameter v_o is the kinematic viscosity of the lubricant in centistrokes and n is the inner race angular velocity in r.p.m. The total friction drag torque T_d for a bearing is the sum of the friction drag torques.

Heat energy is produced by sliding and by the internal drag friction torque. Excessive transient heating may damage the bearing so that calculation of heat energy provides an important performance parameter for CB design. The thermal power loss is calculated as follows:

1. Due to drag torque, $PL_{1j} = T_{dj}\dot{\theta}_{ij}$, $j = 1, 2$, where $T_{dj} = T_{dlj} + T_{dvj}$.

2. Due to sliding at contact points, $PL_{2j} = \vec{F}_{tj} \cdot \vec{V}_{relj}$, where $\vec{V}_{rel}$ is the tangential relative velocity between the inner race and rotor at the contact point. For the $j = 2$ case (bottom bearing), the power loss due to axial sliding, $T_{za}(\omega_r - \dot{\theta}_{i2})$, is added to PL_{2j}. Let the contact point on the rotor be p and that on the inner race be p', then

$$\vec{V}_p = \vec{V}_{o_r} + R_r\dot{\theta}_r\vec{a}_t$$
$$= (\dot{x}\cos\alpha + \dot{y}\sin\alpha)\vec{a}_n + (-\dot{x}\sin\alpha + \dot{y}\cos\alpha)\vec{a}_t + R_r\dot{\theta}_r\vec{a}_t,$$

$$\vec{V}_{p'} = \vec{V}_{o_b} + R_b\dot{\theta}_i\vec{a}_t$$
$$= (\dot{x}_b\cos\alpha + \dot{y}_b\sin\alpha)\vec{a}_n + (-\dot{x}_b\sin\alpha + \dot{y}_b\cos\alpha)\vec{a}_t + R_b\dot{\theta}_i\vec{a}_t,$$

where $\vec{a}_n$ and $\vec{a}_t$ are unit vectors in the normal and tangential directions at the contact point, respectively (see Fig. 2).

$$\text{since } \vec{V}_{rel} = \vec{V}_p - \vec{V}_{p'},$$

$$PL_2 = \vec{F}_t \cdot \vec{V}_{rel} = F_t(R_r\omega_r - R_b\dot{\theta}_i) + F_t[(\dot{x}_b - \dot{x})\sin\alpha + (\dot{y} - \dot{y}_b)\cos\alpha].$$

The total power loss is

$$PL_{total} = \sum_{j=1}^{2}(PL_{1j} + PL_{2j}). \tag{17}$$

The corresponding heat energy is then obtained by integrating the total power loss:

$$\text{Heat energy} = \int_0^t PL_{total}(t)\,\mathrm{d}t. \tag{18}$$

3. Bearing model validation

Accurate prediction of bearing stiffness is crucial in the rotor drop simulation because the bearing stiffness is significantly influenced by the ball centrifugal force when the inner race spin speed is accelerated by the contact force. The bearing stiffness depends on axial preload and the inner race speed and is determined by a bearing Jacobian matrix [15] or stiffness matrix for a 3D bearing model with centrifugal force. A brief explanation on how to obtain the bearing stiffness using this analysis will follow along with a comparison of results with data from another journal paper and a commercial bearing analysis code. Fig. 4 shows a cross-section of the ball bearing with reference coordinates. The inner race is externally loaded by the force vector $\{F\}$ with components in its coordinate system as shown in Fig. 5(a):

$$\{F\}^{\mathrm{T}} = \{F_x, F_y, F_z, M_x, M_y).$$

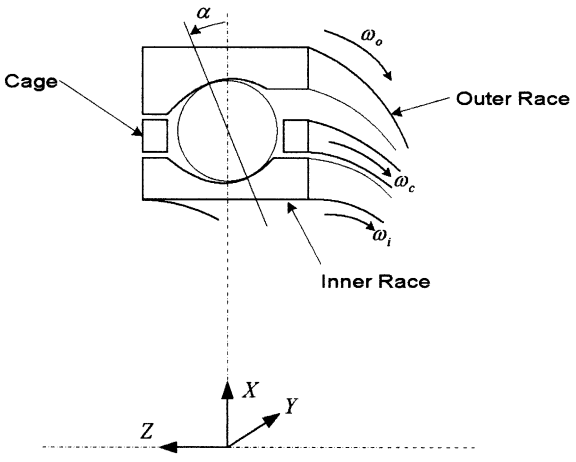

Fig. 4. Cross-section of ball bearing with reference coordinate.

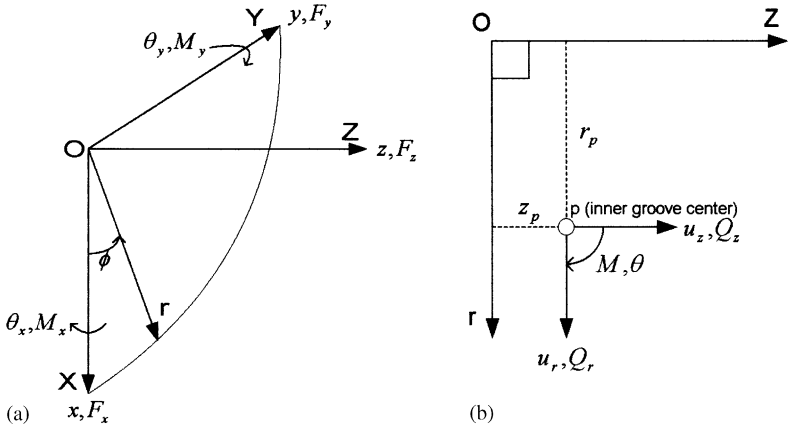

Fig. 5. (a) Ball bearing coordinate system with bearing loads and displacements, (b) inner race cross-section coordinate system with contact loads and displacements.

The corresponding displacement vector $\{X\}$ for the same reference point is

$$\{X\}^{\mathrm{T}} = \{x, y, z, \theta_x, \theta_y\}.$$

Fig. 5(b) shows that the inner race cross-section at a ball is loaded by the contact force vector $\{Q\}$ at the reference point p (inner groove center), which has a displacement vector $\{u\}$. The parameter ϕ is calculated such that the $r-z$ plane passes through the center of the ball

$$\{Q\}^{\mathrm{T}} = \{Q_r, Q_z, M\}, \quad \{u\}^{\mathrm{T}} = \{u_r, u_z, \theta\}.$$

Assuming the displacements are small, the vectors for different reference points are related by the transformation matrix T:

$$\{u\} = T\{X\}, \quad \{Q\} = T\{f\}, \tag{19}$$

where

$$T = \begin{bmatrix} \cos\phi & \sin\phi & 0 & -z_p \sin\phi & z_p \cos\phi \\ 0 & 0 & 1 & r_p \sin\phi & -r_p \cos\phi \\ 0 & 0 & 0 & -\sin\phi & \cos\phi \end{bmatrix}$$

and $\{f\}$ is an equivalent force vector at the inner race reference point with

$$\{f\}^{\mathrm{T}} = \{f_x, f_y, f_z, m_x, m_y\}.$$

The load equilibrium equations for the inner race are

$$\{F\} + \sum_{j=1}^{n} T'\{Q\}_j = \{0\}, \tag{20}$$

where n is number of balls.

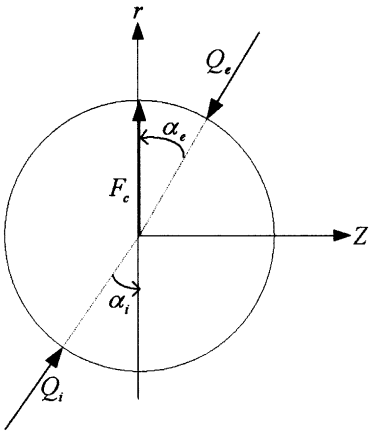

Fig. 6. Ball load equilibrium with centrifugal force.

The ball load equilibrium equations including the centrifugal force F_c are derived from Fig. 6.

$$\begin{Bmatrix} F_r \\ F_z \end{Bmatrix} = \begin{Bmatrix} Q_i \cos\alpha_i - Q_e \cos\alpha_e + F_c \\ Q_i \sin\alpha_i - Q_e \sin\alpha_e \end{Bmatrix} = \begin{Bmatrix} 0 \\ 0 \end{Bmatrix}, \tag{21}$$

where $Q_{i,e}$ are contact loads and $\alpha_{i,e}$ are contact angles.

Since Eqs. (20) and (21) are highly non-linear, the unknown $\{X\}$ and ball center location $\{v\}$ can be solved by a Newton–Raphson method. The linearized form of Eq. (20) is

$$\{F\} + \sum_{j=1}^{n} \{f\}_j + \sum_{j=1}^{n} T_j' \left[\frac{\partial\{Q\}}{\partial\{u\}^{\mathrm{T}}}\right]_j T_j \{\Delta X\} = \{0\}. \tag{22}$$

Eq. (21) is linearized as

$$\begin{Bmatrix} F_r \\ F_z \end{Bmatrix} + \begin{bmatrix} \dfrac{\partial F_r}{\partial v_r} & \dfrac{\partial F_r}{\partial v_z} \\ \dfrac{\partial F_z}{\partial v_r} & \dfrac{\partial F_z}{\partial v_z} \end{bmatrix} \begin{Bmatrix} \Delta v_r \\ \Delta v_z \end{Bmatrix} = \begin{Bmatrix} 0 \\ 0 \end{Bmatrix}. \tag{23}$$

At convergence, the bearing stiffness matrix is represented by

$$\left[\frac{\partial\{F\}}{\partial\{\delta\}^{\mathrm{T}}}\right] = -\sum_{j=1}^{n} T_j' \left[\frac{\partial\{Q\}}{\partial\{u\}^{\mathrm{T}}}\right]_j T_j. \tag{24}$$

The radial and axial stiffness are determined from

$$\text{Radial stiffness} : K_{XX} = -\sum_{j=1}^{n} T' \left[\frac{\partial\{Q\}}{\partial\{u\}^{\mathrm{T}}}\right] T(1,1). \tag{25}$$

$$\text{Axial stiffness} : K_{ZZ} = -\sum_{j=1}^{n} T' \left[\frac{\partial\{Q\}}{\partial\{u\}^{\mathrm{T}}}\right] T(3,3).$$

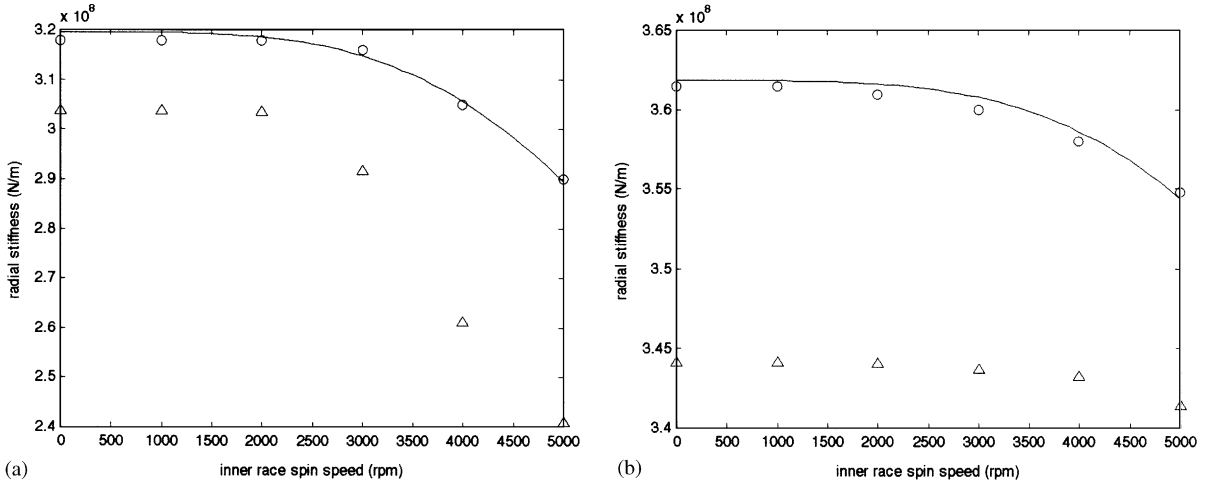

Fig. 7. Bearing radial stiffness comparison (solid, present approach; ○, Ref. [17]; Δ, BASDREL): (a) steel ball, (b) ceramic ball.

The radial stiffness from Eq. (25) is compared with the numerical data from Ref. [17] and a commercial bearing code for model validation. The bearing parameters are given as: F_z (axial preload) = 540 N, F_r (radial load) = 500 N, $\alpha_o = 15^\circ$, $d_m = 0.09$ m, and $n = 20$. Fig. 7 shows the radial stiffness for steel and ceramic ball bearings. A solid line indicates the numerical results from our code, the circle indicates data from Ref. [17] and the triangle data is from the commercial bearing code, BASDREL by Crawford Meeks [20]. The results show a good match with data from two references.

4. Simulation results and discussion

Rotor drop simulations are conducted to illustrate implementation of the high-fidelity CB model and use of the performance indices to identify a good CB design. Numerical integration of the EOM for the flywheel rotor system in Appendix A is performed. The CB dimension and material characteristics are listed in Table 1. Fig. 8 shows the CB stiffness versus inner race spinning speed for different axial preloads. The stiffness is seen to increase as the axial preload increases and it decreases as the inner race spin speed increases.

Table 2 lists the specifications for the shaft, flywheel, motor and CBs. The flywheel and motor have 0.00254 mm imbalance eccentricity with 90° phase difference. When a simulation starts, the flywheel system spins at 40 000 r.p.m. and is axially (Z-axis) dropped down to the bottom CB by gravity and moves from the reference frame center with the initial translational velocity 5 cm/s in X and Y directions. The radial clearance of the CBs is half the MB clearance. A 444.8 N X-axis MB static side load may be applied to the shaft depending on the simulation case.

A numerical solution is obtained using a variable time-step fourth order Runge–Kutta integration algorithm. The total integration time is 1 s and the display time step is 4×10^{-5} s. To treat contact status, calculate the relative distance, s between the rotor and inner race geometric

Table 1
Specifications of catcher bearings

Dimension	Specification
Geometric specification	
Bore diameter, BD	1.7 cm
Outside diameter, OD	3.5 cm
Width	1.0 cm
Inner and outer race groove radius	2.083 and 2.144 mm
Number of balls	16
Diameter of a ball	3.969 mm
Initial contact angle	15°
Axial preload	88.964 N
Number of rows	2
Material specification	
Density of ball: ceramic	3.2 g/cm^3
Density of inner and outer race: steel	7.8 g/cm^3
Elastic modulus of ball	290 GPa
Poisson ratio of ball	0.26
Elastic modulus of inner and outer race	208 GPa
Poisson ratio of inner and outer race	0.3
Lubricant	
Viscosity	50 Cst

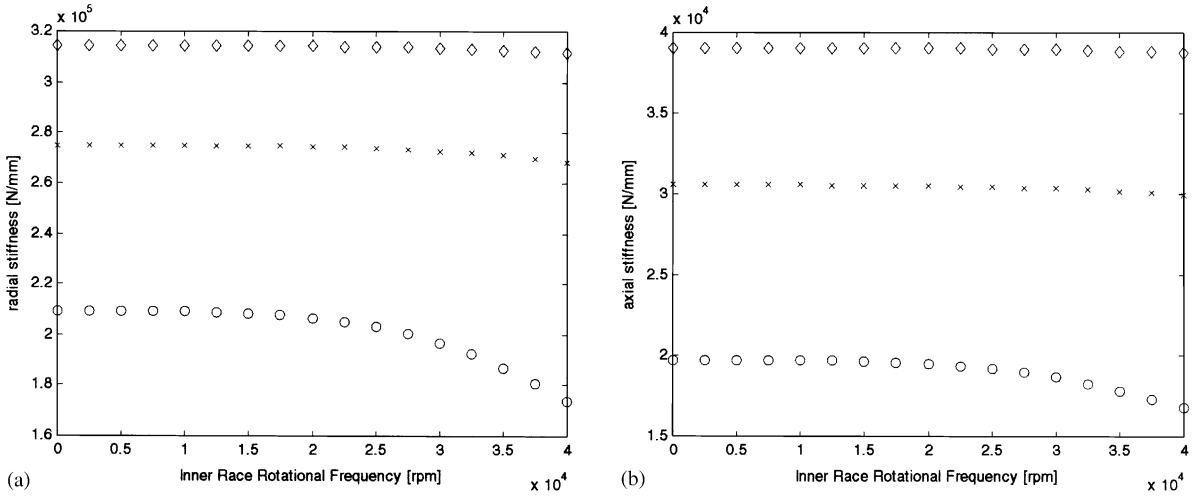

Fig. 8. CB stiffness depending on inner race speed and axial preload (○, 89 N; ×, 222 N; ◇, 356 N): (a) radial stiffness, (b) axial stiffness.

centers from Eq. (2). If the distance is greater than the nominal CB clearance, the normal and tangential contact forces are applied to the rotor and inner race. If the distance is less than the clearance, the contact forces become zero in the simulation program. Theoretically, rolling

Table 2
Specifications of simulation models

Dimension	Specification
Shaft	
Mass	2.39 kg
Polar MOI, I_{ps}	0.0011 kg m^2
Transverse MOI, I_{ts}	0.0087 kg m^2
Radial clearance of MBs	0.508 mm
Radial clearance of CBs	0.254 mm
Flywheel	
Mass	26.71 kg
Polar MOI, I_{pf}	0.7237 kg m^2
Transverse MOI, I_{tf}	0.4460 kg m^2
Unbalance eccentricity, e_f	0.00254 mm
Motor	
Mass	2.65 kg
Polar MOI, I_{pm}	0.0060 kg m^2
Transverse MOI, I_{tm}	0.0033 kg m^2
Unbalance eccentricity, e_m	0.00254 mm
Total	
Polar MOI, I_{pt}	0.7308 kg m^2
Initial spinning speed, p	40 000 r.p.m.
Catcher bearing	
Mass of inner race	0.104 kg
Mass of outer race	0.615 kg
Polar MOI of inner race, I_{pb}	1.24E-4 kg m^2
Axial initial height, δ_{drop}	0.381 mm
Damping coefficient of CB, C_{ba} and C_b	200 N s/m
Axial support stiffness, K_{sa}	3.5E + 6 N/m
Axial support damping coefficient, C_{sa}	1.75E + 4 N s/m
Radial support stiffness, K_s	3.5E + 6 N/m
Radial support damping coefficient, C_s	See Table 3
Dynamic friction coefficient of CB	See Table 3
Static friction coefficient of CB	See Table 3
Axial preloads, F_a	See Table 3
X-axis side loads from MBs, F_{sl}	See Table 3

happens when the tangential velocities of the rotor and inner race are exactly the same, but numerically, this may not happen. Furthermore, the tangential force is very high when backward whirl happens and it changes direction whenever the relative tangential velocity changes direction. Thus a very small boundary (1E-8) is added around zero relative velocity and if the relative velocity is within this boundary, the rolling condition is applied to determine tangential contact force and if the relative velocity exceeds this boundary, a slipping condition is applied.

In order to investigate the effects of the CB design parameters on the rotor dynamics, the parameter studies are performed for CB axial preload (F_a), friction coefficient of the shaft/inner race interface ($\mu_{s,d}$), the radial support damping coefficient of the damper liner (C_s), and X-axis side loads from the MBs (F_{sl}). The last parameter may be useful in the event that MB control is lost, however the MB actuator remains operative.

The following performance indices (PIs) are developed to compare and characterize the simulation responses: (1) peak radial normal contact force (N); (2) peak axial normal contact force (N); (3) peak impulse due to radial normal contact force (N s); (4) peak impulse due to axial normal contact force (N s); (5) shaft speed decrease (r.p.m.); (6) final inner race speed (r.p.m.); (7) maximum power loss due to drag torque (W); (8) maximum power loss due to contact force with rotor (W); (9) maximum total power loss (W); (10) maximum heat energy due to drag torque (J); (11) maximum heat energy due to contact force with rotor (J); (12) maximum total heat energy (J); (13) final rotor whirl rate at top CB (r.p.m.); (14) final rotor whirl rate at bottom CB (r.p.m.); (15) minimum air gap at MBs (mm).

The first PI indicates the maximum contact normal force on either of the top and bottom inner races on $X-Y$ plane, while the second PI is the maximum axial contact normal force on the bottom CB. These two PIs are important for CB life prediction. The third and fourth PIs are impulses due to the PI_1 and PI_2. The fifth and sixth indices represent the shaft speed decrease and increase of the CB speed, respectively. The seventh to 12th indices denote the maximum power loss due to bearing drag torque and contact friction with rotor, and the maximum heat energy, which is the time integral of the power loss. The 13th and 14th indices show the final shaft whirl rate at the CBs. The minimum air gap at MBs, the last index, represents how much radial air gap is available at the MB locations (how safe MB stators are), which is equal to 0.508 mm minus the maximum radial motion of the rotor at the MBs.

Table 3 shows the simulation cases presented here. The PIs from the last four simulations of Case I will be compared with those of Case IV to investigate the effects of side load.

Figs. 9–20 show the simulation results for Case I-2 in Table 3. The rotor motions at the CB locations are plotted in Figs. 9 and 10. Fig. 9 shows that the rotor motion is damped out by the damper liner. From the orbit plot, it is observed that the X-axis side loads mainly move the rotor along the X-axis. The dynamic responses of the inner and outer races are shown in Figs. 11 and 12.

Fig. 13 shows the angular velocities of the rotor shaft and inner races, and rotor whirl rate. In Fig. 13(b), the bottom CB is accelerated faster than the top one because the axial and radial contacts produce more driving torque. It can be noticed from Fig. 13(c) and (d) that the rotor whirl rate reverses sign because it oscillates on the inner races along the Y direction (refer to Fig. 10).

The angles at contacts, and normal and tangential (friction) contact forces at the inner races are presented in Fig. 14. Fig. 14 shows that contact is intermittent. The variable integration time step is found to decrease much smaller than the contact duration during contact events. The radial normal contact force reaches 3000 N for the first hit and remains under 600 N.

Fig. 15 shows the impulse due to the normal contact force. Power loss in the CBs is presented in Fig. 16. It can be noticed that the power loss due to the friction force between the rotor and inner race is dominant compared with the power loss due to drag torque.

Table 3
Simulation cases

Simulation no.	μ_s, μ_d	F_a (N)	C_s (N s/mm)	F_{sl} (N)
Case I: friction coefficient effects				
I-1	0.2, 0.05	88.96	87.6	444.82
I-2	0.3, 0.1	88.96	87.6	444.82
I-3	0.4, 0.2	88.96	87.6	444.82
I-4	0.45, 0.25	88.96	87.6	444.82
I-5	0.5, 0.3	88.96	87.6	444.82
Case II: axial preload effects				
II-1	0.4, 0.2	88.96	87.6	0
II-2	0.4, 0.2	222.41	87.6	0
II-3	0.4, 0.2	355.86	87.6	0
Case III: support damper effects				
III-1	0.3, 0.1	88.96	0.876	0
III-2	0.3, 0.1	88.96	1.75	0
III-3	0.3, 0.1	88.96	3.50	0
III-4	0.3, 0.1	88.96	8.76	0
III-5	0.3, 0.1	88.96	17.5	0
III-6	0.3, 0.1	88.96	43.8	0
III-7	0.3, 0.1	88.96	87.6	0
Case IV: side load effects				
IV-1	0.3, 0.1	88.96	87.6	0
IV-2	0.4, 0.20	88.96	87.6	0
IV-3	0.45, 0.25	88.96	87.6	0
IV-4	0.5, 0.3	88.96	87.6	0

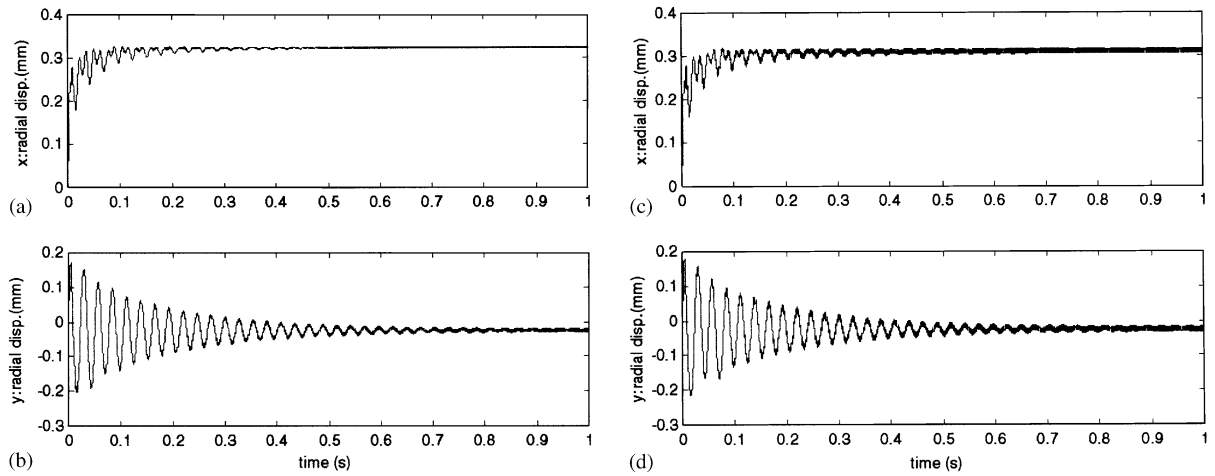

Fig. 9. Dynamic response of the rotor (a) at the top CB in X-axis, (b) at the top CB in Y-axis, (c) at the bottom CB in X-axis, and (d) at the bottom CB in Y-axis.

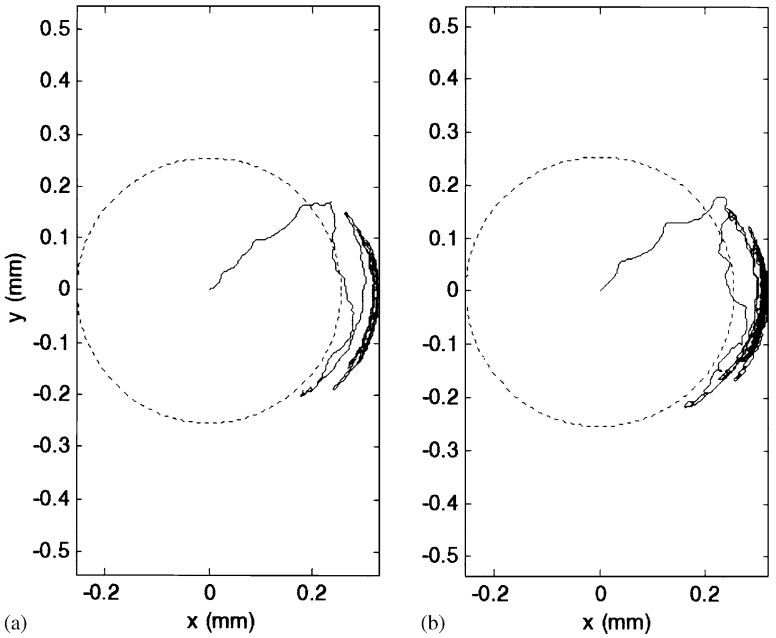

Fig. 10. Orbit plot of the rotor (dashed, CB clearance): (a) at the top CB and (b) at the bottom CB.

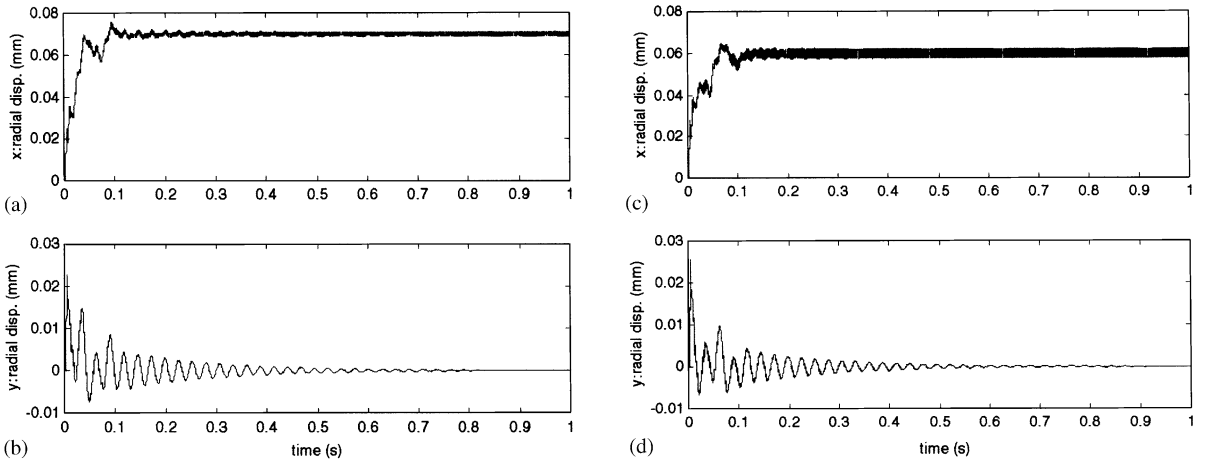

Fig. 11. Dynamic response of the inner race (a) at the top CB in X-axis, (b) at the top CB in Y-axis, (c) at the bottom CB in X-axis, and (d) at the bottom CB in Y-axis.

Fig. 17 shows the heat energy in the CBs categorized by sources: drag torque and friction force. The friction force between the rotor and inner race is again the major source for the total heat energy. The total energy transferred to the CBs including kinetic energy of the inner races, and dissipated energy by the damper liner and the flexible hubs is compared to the kinetic energy drop of the spinning flywheel system in Fig. 18. Fig. 18(b) shows the consistent match with about 4 J difference at the final time. Fig. 19 shows the axial motions of the shaft, inner race and outer race

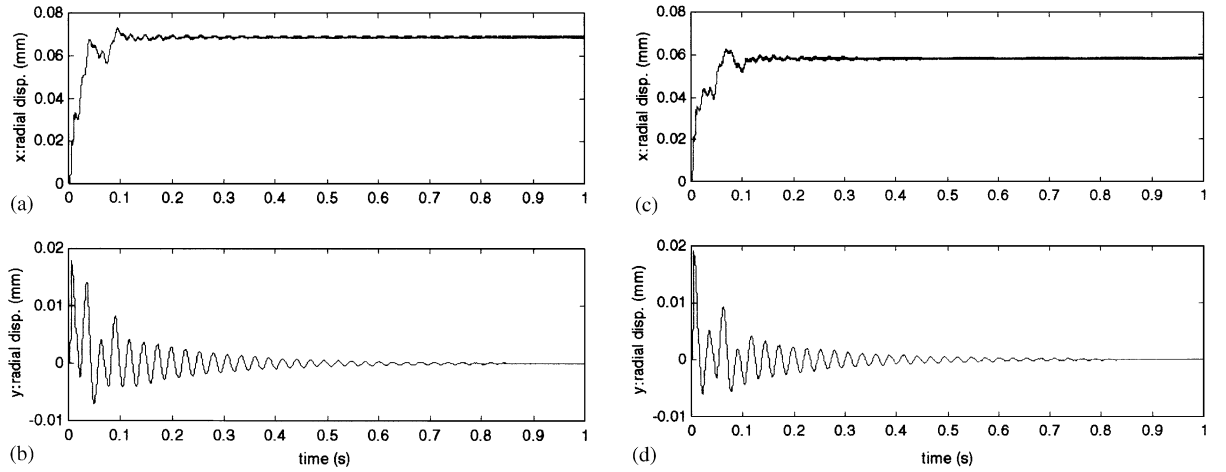

Fig. 12. Dynamic response of the outer race (a) at the top CB in X-axis, (b) at the top CB in Y-axis, (c) at the bottom CB in X-axis, and (d) at the bottom CB in Y-axis.

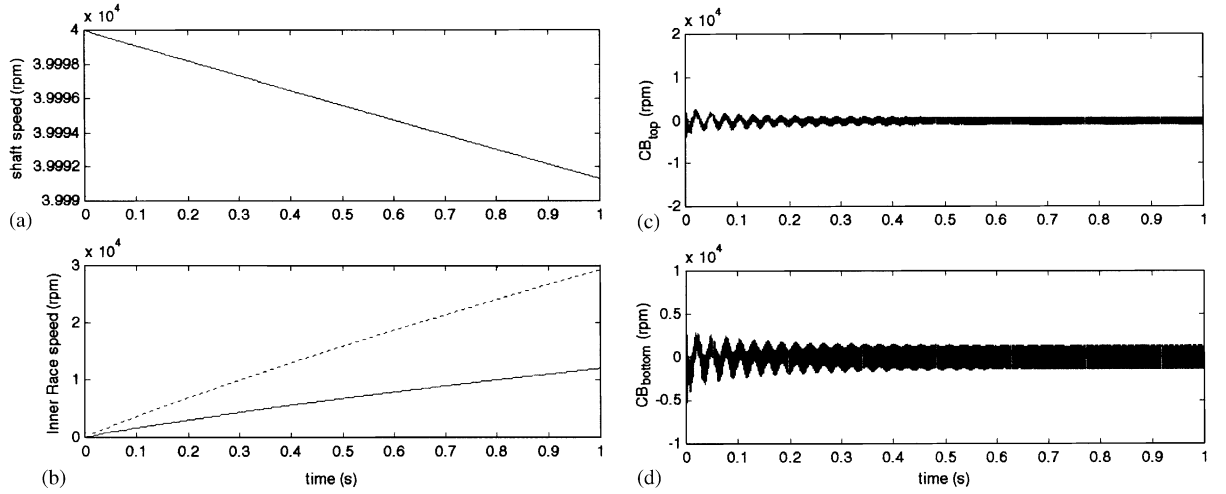

Fig. 13. (a) Rotor spin speed, (b) inner race spin speed (solid, top CB; dashed, bottom CB), rotor whirl rate (c) at the top CB and (d) at the bottom CB.

which go to steady state after an overshoot. The axial normal force on the bottom CB and the corresponding impulse are shown in Fig. 20.

Figs. 21 and 22 show the dynamic responses for Case I-5 with $\mu_s = 0.5$ and $\mu_d = 0.3$. The orbit plot of the rotor at CBs in Fig. 21 show that the rotor whirls due to high friction coefficient even under the side load.

It can be observed from Fig. 22 that the rotor whirl rate transiently reaches $-40\,000$ r.p.m. and then the high-frequency backward whirl is diminished by the support damping.

Table 4 shows the PIs obtained from the simulation results for Case I. For the PIs 13 and 14, these results are for the end of the 1-s transient simulation. It is observed that the peak radial

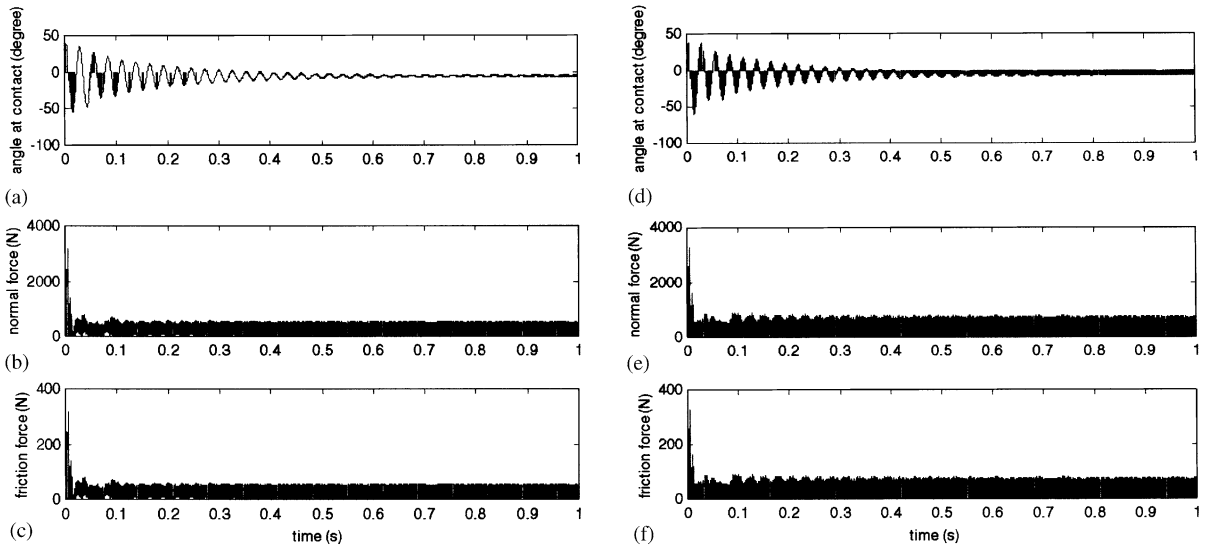

Fig. 14. Angle at contact (a) in the top CB and (d) in the bottom CB, contact normal force (b) in the top CB and (e) in the bottom CB, and contact tangential force (c) in the top CB and (f) in the bottom CB.

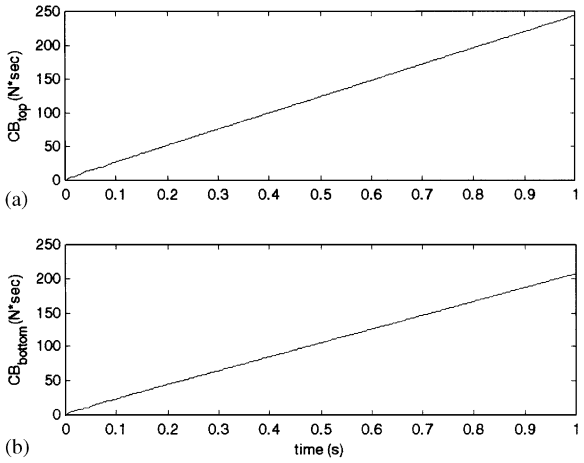

Fig. 15. Impulse due to radial normal force (a) at the top CB and (b) at the bottom CB.

contact force, the first PI, and the peak impulse, the third PI, rapidly increase between Case I-4 and Case I-5. This is because the high frequency backward whirl occurs in Case I-5. The maximum power loss, the 9th PI, and the maximum heat energy, the 12th PI, increase as the friction coefficient increases. The minimum air gap at the MBs, the last PI, significantly decreases between Case I-4 and Case I-5. Although the peak radial contact force for Case I-5 is 9387 N, this diminishes to 908 N at the end of the 1 s simulation interval. Figs. 23 and 24 summarize the effects of dynamic friction coefficient on the key PIs.

The axial preload is an important design parameter in CB design. From Fig. 8, it was verified that the more the axial preload is applied the more bearing stiffness is obtained. Table 5 shows the

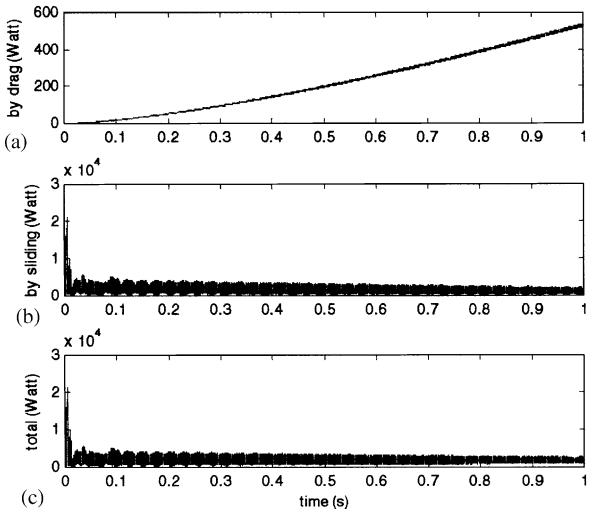

Fig. 16. (a) Power loss due to drag torque in CBs, (b) power loss due to contact tangential force in CBs, (c) total power loss in CBs.

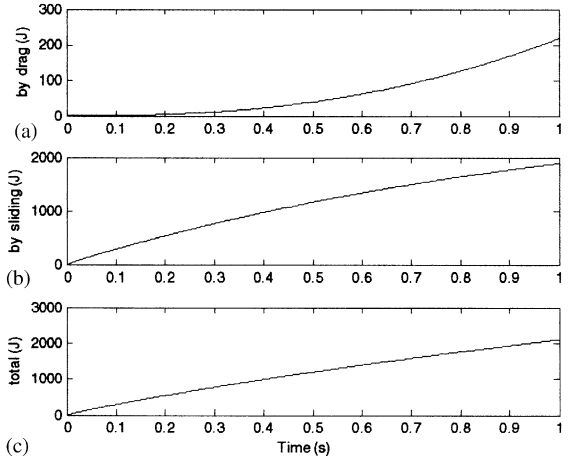

Fig. 17. (a) Heat energy loss due to drag torque in CBs, (b) heat energy loss due to contact tangential force in CBs, (c) total heat energy loss in CBs.

PIs from the simulation results for Case II. The peak radial contact force and the corresponding peak impulse are increased as the axial preload is increased. The minimum MB air gap is also increased as more preload is applied but not significantly.

The total power loss and energy loss, the 9th and 12th PIs, increase as the axial preload is increased. Since more preload induces more drag torque the appropriate axial preload amount is important in the sense that the power loss due to an excessive preload can result in bearing seizure and too little preload can soften the CB and cause loss in the MB air gap. The key PIs versus axial preload are shown in Figs. 25 and 26.

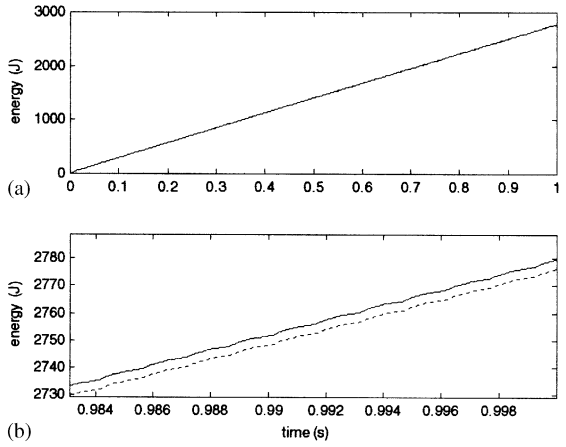

Fig. 18. (a) Energy balance, (b) scaled plot (solid, flywheel energy drop; dashed, total energy transferred to CBs).

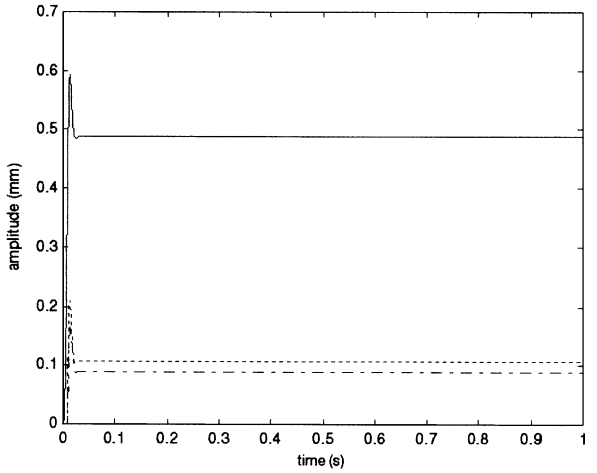

Fig. 19. Axial motion of shaft, inner race and outer race (solid, rotor; dashed, inner race; dashdot, outer race).

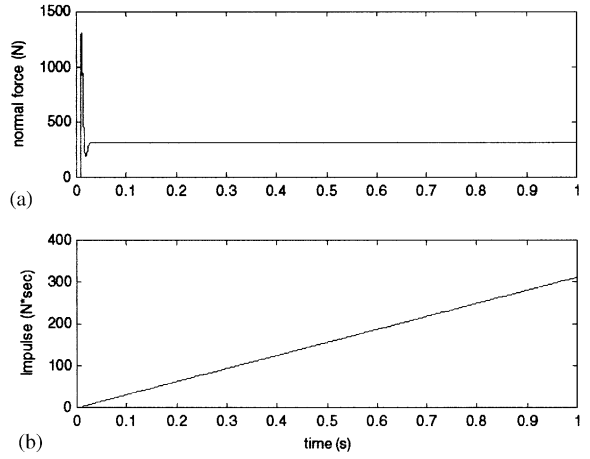

Fig. 20. (a) Axial normal force, (b) impulse due to axial normal force.

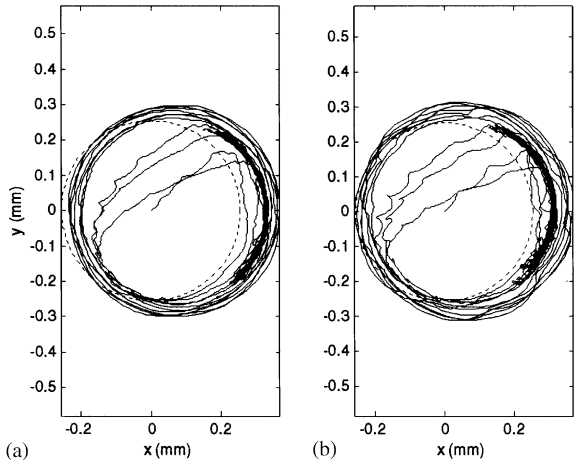

Fig. 21. Orbit plot of the rotor for Case I-5 (dashed, CB clearance): (a) at the top CB and (b) at the bottom CB.

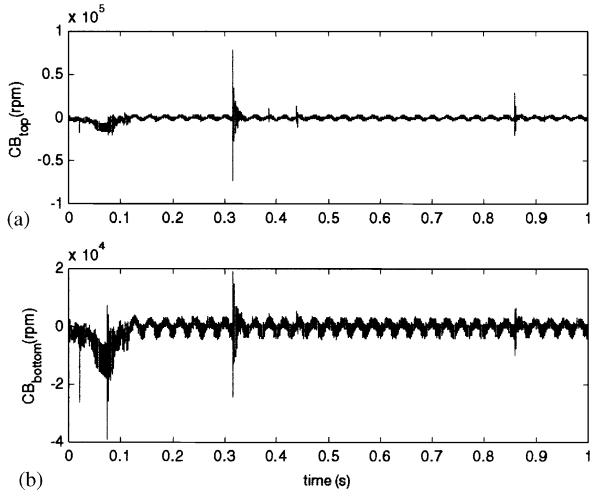

Fig. 22. Rotor whirl rate for Case I-5: (a) at the top CB and (b) at the bottom CB.

A PI summary for Case III is shown in Table 6. The peak contact force decreases up to Case III-3 and increases as shown in Fig. 27(a). This illustrates that a given rotor drop system has an optimum damping. This result is consistent with what Ishii and Kirk pointed out in Ref. [2]. The peak impulse in Fig. 27(b) has a similar trend as the peak force but it has a minimum value at Case III-5. The minus minimum air gap obtained from Case III-1 indicates that the rotor hits the MB stator. Fig. 27(c) shows that the air gap sharply increases from III-1 to III-5 and is nearly unaffected by C_s above 10 N s/mm.

As shown in Fig. 28, the total power loss is decreased until Case III-3 and is sharply increased after that due to the friction force between the rotor and CBs, while the energy loss has the minimum value at Case III-5 and gradually increases. Several design objectives can be considered

Table 4
Performance indices for Case I

PI	I-1	I-2	I-3	I-4	I-5
1	3253 N	3264	3268	3256	9387
2	1294 N	1311	1296	1293	1295
3	244.15 N s	243.66	242.78	262.61	471.85
4	311.13 N s	311.16	311.16	311.15	311.48
5	4.34 r.p.m.	8.66	13.52	15.51	17.17
6	13 762 r.p.m.	29 208	39 283	39 424	39 441
7	153.4 W	538.6	1042.4	1303.3	1522.2
8	10 509 W	20 993	41 783	52 018	88 698
9	10 684 W	21 170	41 965	52 204	90 096
10	63.3 J	216.7	575.0	707.7	1283.4
11	1177.2 J	1884.9	2280.0	2369.9	2156.2
12	1241.6 J	2102.6	2856.2	3079.6	3471.6
13	653 r.p.m.	607	1100	−1839	822
14	−1222 r.p.m.	−920	−37	638	−1776
15	0.183 mm	0.182	0.174	0.173	0.139

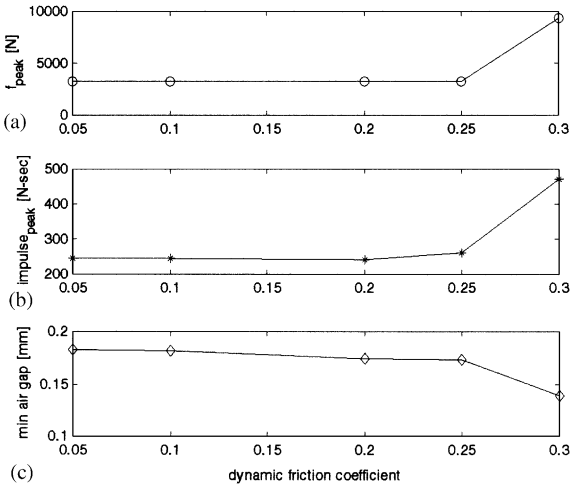

Fig. 23. For Case I, (a) peak radial contact force versus μ_d, (b) peak impulse versus μ_d, (c) minimum air gap versus μ_d.

to find an optimum damping. Enough air gap at the MBs has to be guaranteed, and the peak contact force and impulse have to be reduced. The minimum peak contact force is obtained in Case III-3 but the maximum air gap is not. Minimizing heat energy is another design objective. The final whirl direction and amount are also important to avoid excessive backward whirl. Cases III-1, 2, 6, and 7 results showed backward whirls with over 1000 r.p.m. at both CBs.

Figs. 29 and 30 compare the PIs with and without side loads. From Fig. 29(a), it can be noticed that the peak normal force is gradually increased in the case without side loads but in the case with side loads, it is almost constant before backward whirl occurs. The peak impulse is higher, the

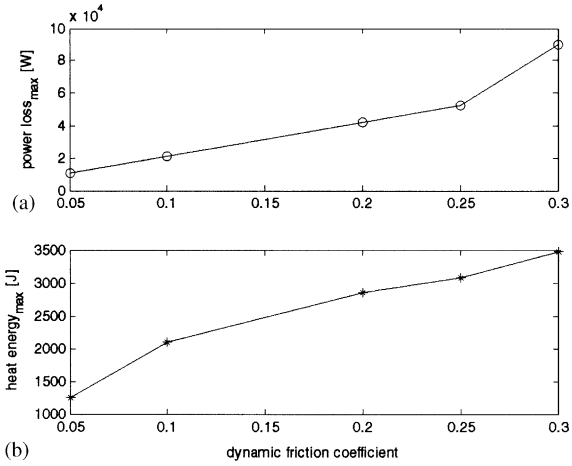

Fig. 24. For Case I, (a) maximum power loss versus μ_d, (b) maximum heat energy versus μ_d.

Table 5
Performance indices for Case II

PI	II-1	II-2	II-3
1	4917 N	5810	6324
2	1316 N	1461	1518
3	550.74 N s	554.12	560.53
4	311.16 N s	311.17	311.16
5	16.93 r.p.m.	17.07	17.25
6	39 708 r.p.m.	39 699	39 688
7	1389.0 W	1446.3	1512.6
8	38 992 W	40 593	40 812
9	39 502 W	41 172	41 415
10	1228.1 J	1266.4	1316.3
11	2105.1 J	2112.0	2119.6
12	3357.4 J	3403.6	3460.9
13	−2143.9 r.p.m.	−1729.6	−1218.4
14	−2249.1 r.p.m.	−1148.2	−3346.7
15	0.22 mm	0.222	0.23

minimum air gap is lower and more heat energy is generated in the case without side loads. More heat energy in the CBs is generated in the case without side loads.

5. Conclusions

The detailed CB mathematical model, which includes power loss, a Hertzian load–deflection non-linear relationship and inner race speed-and-axial preload-dependent bearing stiffness, was developed in this paper. Inner race speed and axial preload-dependent bearing stiffness is an

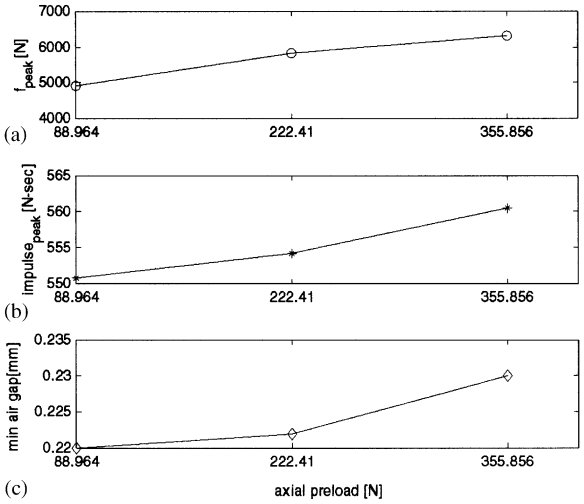

Fig. 25. For Case II, (a) peak radial contact force versus axial preload, (b) peak impulse versus axial preload, (c) maximum air gap versus axial preload.

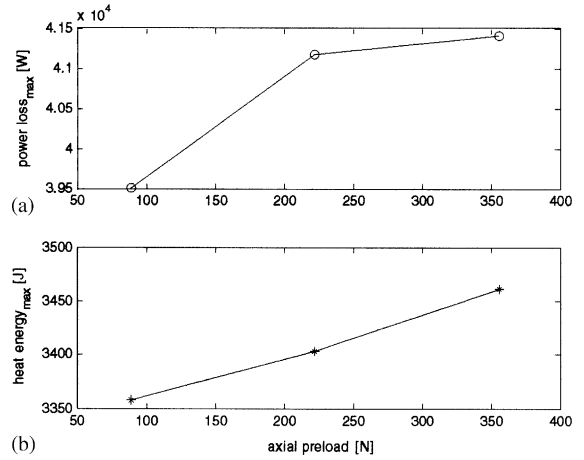

Fig. 26. For Case II, (a) maximum power loss versus axial preload, (b) maximum heat energy versus axial preload.

important factor in high speed CB applications, i.e. the accelerated inner race speed in this study reached about 40 000 r.p.m. The drop test of the vertical shaft rotor with the flywheel and motor combined was numerically performed with a variety of design parameters of CBs such as dynamic friction coefficient, axial preload, support damping, and side load and analyzed using 15 performance indices (PI).

The simulation results show that as the friction coefficient is increased, the peak normal force and the corresponding impulse increase, while the minimum air gap decreases. Fully developed backward whirl occurs at $\mu_d = 0.3$ even with the side loads.

Table 6
Performance indices for Case III

PI	III-1	III-2	III-3	III-4	III-5	III-6	III-7
1	1078.5 N	834.9	813.7	996.7	1242.4	1710.3	2012.6
2	1310.2 N	1325.7	1313.9	1319.5	1323.4	1324.8	1321.5
3	665 N s	454	283	88.5	65.3	244.4	467.5
4	311.16 N s	311.16	311.16	311.16	311.16	311.16	311.16
5	15.17 r.p.m.	12.72	9.88	5.70	5.18	8.63	13.03
6	38793 r.p.m.	38 794	33 923	22 548	21 266	29 549	39 392
7	1295.8 W	997.4	686.3	290.3	258.2	550.4	1057.8
8	5692.9 W	5363.9	5120.1	5144.6	6851.2	9480.9	11 933
9	5699.9 W	5368.2	5122.1	5146.2	6919.1	9545.1	11 998
10	634.1 J	415.2	243.1	123.1	106.3	183.8	451.4
11	2310.9 J	2236.5	1991.3	1347.1	1242.1	1874.7	2201.6
12	2953.6 J	2658.0	2238.4	1471.6	1349.3	2062.5	2662.6
13	−2913 r.p.m.	−1319	−3389	288	−945	−1869	−3427
14	−1459 r.p.m.	−2874	−590	−1247	32	−4299	−2028
15	0.05 mm	0.073	0.126	0.176	0.202	0.220	0.227

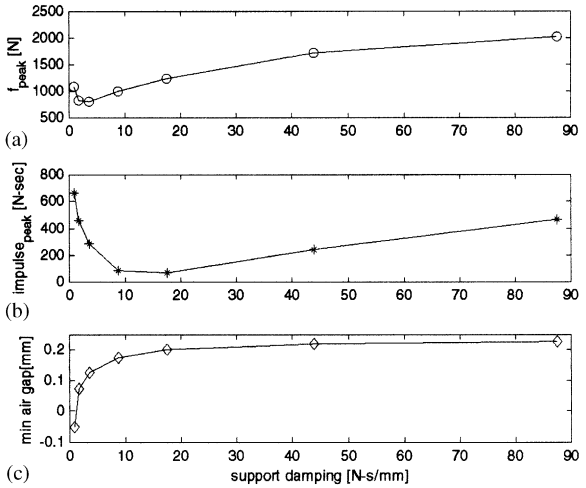

Fig. 27. For Case III, (a) peak radial contact force versus support damping, (b) peak impulse versus support damping, (c) maximum air gap versus support damping.

The power loss and heat energy increases as the friction coefficient increase. The peak normal force and impulse increase, and a slightly more minimum air gap is obtained as the axial preload is increased. The peak normal force decreases and then increases after having a minimum value at 3.50 N s/mm as the support damping is increased. The peak impulse has the same trend as the peak normal force but has a minimum value at a support damping of 17.5 N s/mm. The minimum air gap increases and becomes almost constant above $C_s = 43.8$ N s/mm. The side loads help reduce the peak normal force, impulse and heat energy but result in less minimum air

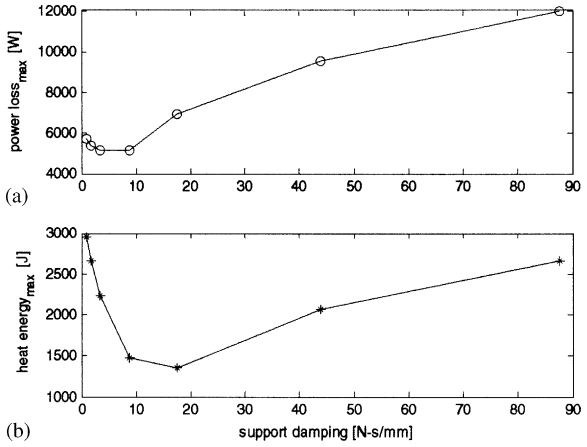

Fig. 28. For Case III, (a) maximum power loss versus support damping, (b) maximum heat energy versus support damping.

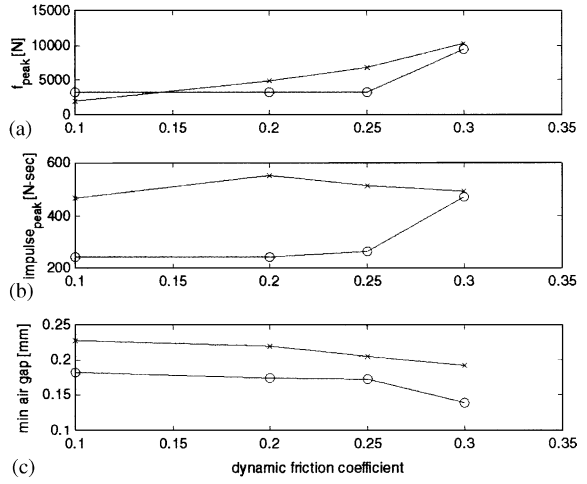

Fig. 29. For Case IV (○, with side loads; ×, without side loads), (a) peak radial contact force versus μ_d, (b) peak impulse versus μ_d, (c) minimum air gap versus μ_d.

gap. In this paper, only results for a soft support stiffness ($K_s = 3.5\text{E}+6\,\text{N/m}$) are reported but in rigid support stiffness cases ($K_s = 8.76\text{E}+8\,\text{N/m}$), the side loads make the minimum air gap increase because they prevent the rotor from entering into a destructive backward whirl.

Although the model utilized in this study is significantly more detailed than its counterparts in previous CB papers, it will be enhanced to include individual ball motion, stress calculation on balls, thermal expansion, temperature-dependent lubricant viscosity, wear and life prediction in our planned future work. In addition, the analytical results will be benchmarked against test results from a recently completed, experimental CB rig at NASA Glenn.

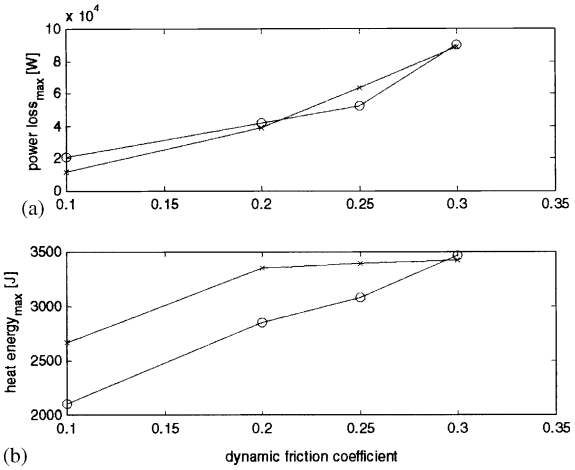

Fig. 30. For Case IV (○, with side loads; ×, without side loads), (a) maximum power loss versus μ_d, (b) maximum heat energy versus μ_d.

Acknowledgements

We gratefully acknowledge support of this research by NASA Glenn grants NRA-GRC-99-02 and NRA-99-OSS-05.

Appendix A. Equations of motion for the simulation model

From Fig. 1, the motor motion is described as

$$\begin{aligned} M_m\ddot{x}_m = & -K_{mtxx}(x_m - x_r - d_1\theta_{ry}) - C_{mtx}(\dot{x}_m - \dot{x}_r - d_1\dot{\theta}_{ry}) \\ & - K_{mtxy}(y_m - y_r + d_1\theta_{rx}) + M_m e_m \omega_z^2 \cos(\omega_z t), \end{aligned}$$

$$\begin{aligned} M_m\ddot{y}_m = & -K_{mtyy}(y_m - y_r + d_1\theta_{rx}) - C_{mty}(\dot{y}_m - \dot{y}_r + d_1\dot{\theta}_{rx}) \\ & - K_{mtyx}(x_m - x_r - d_1\theta_{ry}) + M_m e_m \omega_z^2 \sin(\omega_z t), \end{aligned}$$

$$\begin{aligned} I_{mt}\ddot{\theta}_{mx} = & -I_{mp}\omega_z\dot{\theta}_{my} - K_{mrxx}(\theta_{mx} - \theta_{rx}) \\ & - C_{mrx}(\dot{\theta}_{mx} - \dot{\theta}_{rx}) - K_{mrxy}(\theta_{my} - \theta_{ry}), \end{aligned}$$

$$I_{mt}\ddot{\theta}_{my} = I_{mp}\omega_z\dot{\theta}_{mx} - K_{mryy}(\theta_{my} - \theta_{ry}) - C_{mry}(\dot{\theta}_{my} - \dot{\theta}_{ry}) - K_{mryx}(\theta_{mx} - \theta_{rx}),$$

where K_{mtxx} and K_{mtyy} are translational stiffness of the flexible hub, C_{mtx} and C_{mty} are translational damping of the hub, K_{mtxy} and K_{mtyx} are translational cross-coupled stiffness, K_{mrxy} and K_{mryx} are rotational cross-coupled stiffness, and d_1 is the distance between the motor and rotor mass centers.

Similarly, the flywheel motion is described as

$$\begin{aligned} M_f\ddot{x}_f = & -K_{ftxx}(x_f - x_r - d_2\theta_{ry}) - C_{ftx}(\dot{x}_f - \dot{x}_r - d_2\dot{\theta}_{ry}) \\ & - K_{ftxy}(y_f - y_r + d_2\theta_{rx}) - M_f e_f \omega_z^2 \sin(\omega_z t), \end{aligned}$$

$$\begin{aligned} M_f\ddot{y}_f = & -K_{ftyy}(y_f - y_r + d_2\theta_{rx}) - C_{fty}(\dot{y}_f - \dot{y}_r + d_2\dot{\theta}_{rx}) \\ & - K_{ftyx}(x_f - x_r - d_2\theta_{ry}) + M_f e_f \omega_z^2 \cos(\omega_z t), \end{aligned}$$

$$I_{ft}\ddot{\theta}_{fx} = -I_{fp}\omega_z\dot{\theta}_{fy} - K_{frxx}(\theta_{fx} - \theta_{rx}) - C_{frx}(\dot{\theta}_{fx} - \dot{\theta}_{rx}) - K_{frxy}(\theta_{fy} - \theta_{ry}),$$

$$I_{ft}\ddot{\theta}_{fy} = I_{fp}\omega_z\dot{\theta}_{fx} - K_{fryy}(\theta_{fy} - \theta_{ry}) - C_{fry}(\dot{\theta}_{fy} - \dot{\theta}_{ry}) - K_{fryx}(\theta_{fx} - \theta_{rx}),$$

where d_2 is the distance between the flywheel and rotor mass centers.

The equations of motion (EOMs) for the rotor are

$$\begin{aligned} M_r\ddot{x}_r = & K_{mtxx}(x_m - x_r - d_1\theta_{ry}) + C_{mtx}(\dot{x}_m - \dot{x}_r - d_1\dot{\theta}_{ry}) \\ & + K_{mtxy}(y_m - y_r + d_1\theta_{rx}) + K_{ftxx}(x_f - x_r - d_2\theta_{ry}) \\ & + C_{ftx}(\dot{x}_f - \dot{x}_r - d_2\dot{\theta}_{ry}) + K_{ftxy}(y_f - y_r + d_2\theta_{rx}) \\ & - F_{n1}\cos(\alpha_1) + F_{t1}\sin(\alpha_1) - F_{n2}\cos(\alpha_2) + F_{t2}\sin(\alpha_2) + F_{sl}, \end{aligned}$$

$$\begin{aligned} M_r\ddot{y}_r = & K_{mtyy}(y_m - y_r + d_1\theta_{rx}) + C_{mty}(\dot{y}_m - \dot{y}_r + d_1\dot{\theta}_{rx}) \\ & + K_{mtyx}(x_m - x_r - d_1\theta_{ry}) + K_{ftyy}(y_f - y_r + d_2\theta_{rx}) \\ & + C_{fty}(\dot{y}_f - \dot{y}_r + d_2\dot{\theta}_{rx}) + K_{ftyx}(x_f - x_r - d_2\theta_{ry}) \\ & - F_{n1}\sin(\alpha_1) - F_{t1}\cos(\alpha_1) - F_{n2}\sin(\alpha_2) - F_{t2}\cos(\alpha_2), \end{aligned}$$

$$\begin{aligned} I_{rt}\ddot{\theta}_{rx} = & -I_{rp}\omega_z\dot{\theta}_{ry} - d_1[K_{mtyy}(y_m - y_r + d_1\theta_{rx}) + C_{mty}(\dot{y}_m - \dot{y}_r + d_1\dot{\theta}_{rx}) \\ & + K_{mtyx}(x_m - x_r - d_1\theta_{ry})] - d_2[K_{ftyy}(y_f - y_r + d_2\theta_{rx}) \\ & + C_{fty}(\dot{y}_f - \dot{y}_r + d_2\dot{\theta}_{rx}) + K_{ftyx}(x_f - x_r - d_2\theta_{ry})] \\ & + l_1[-F_{n1}\sin(\alpha_1) - F_{t1}\cos(\alpha_1)] - l_2[-F_{n2}\sin(\alpha_2) - F_{t2}\cos(\alpha_2)] \\ & + K_{mrxx}(\theta_{mx} - \theta_{rx}) + C_{mrx}(\dot{\theta}_{mx} - \dot{\theta}_{rx}) + K_{mrxy}(\theta_{my} - \theta_{ry}) \\ & + K_{frxx}(\theta_{fx} - \theta_{rx}) + C_{frx}(\dot{\theta}_{fx} - \dot{\theta}_{rx}) + K_{frxy}(\theta_{fy} - \theta_{ry}), \end{aligned}$$

$$\begin{aligned} I_{rt}\ddot{\theta}_{ry} = & I_{rp}\omega_z\dot{\theta}_{rx} + d_1[K_{mtxx}(x_m - x_r - d_1\theta_{ry}) \\ & + C_{mtx}(\dot{x}_m - \dot{x}_r - d_1\dot{\theta}_{ry}) + K_{mtxy}(y_m - y_r + d_1\theta_{rx})] \\ & + d_2[K_{ftxx}(x_f - x_r - d_2\theta_{ry}) \\ & + C_{ftx}(\dot{x}_f - \dot{x}_r - d_2\dot{\theta}_{ry}) + K_{ftxy}(y_f - y_r + d_2\theta_{rx})] \\ & - l_1[-F_{n1}\cos(\alpha_1) + F_{t1}\sin(\alpha_1)] + l_2[-F_{n2}\cos(\alpha_2) + F_{t2}\sin(\alpha_2)] \\ & + K_{mryy}(\theta_{my} - \theta_{ry}) + C_{mry}(\dot{\theta}_{my} - \dot{\theta}_{ry}) + K_{mryx}(\theta_{mx} - \theta_{rx}) \\ & + K_{fryy}(\theta_{fy} - \theta_{ry}) + C_{fry}(\dot{\theta}_{fy} - \dot{\theta}_{ry}) + K_{fryx}(\theta_{fx} - \theta_{rx}), \end{aligned}$$

$$I_p\ddot{\theta}_z = -(F_{t1} + F_{t2})R_r - T_{za},$$

where F_{n1} and F_{n2} are the radial normal contact forces between the rotor and inner race, F_{t1} and F_{t2} are the friction forces induced by the contact force, l_1 and l_2 are the distances between the rotor mass center and CBs, and I_p is the polar moment of inertia of the total flywheel system.

From Fig. 2, the EOMs for the top CB are

$$M_{i1}\ddot{x}_{i1} = F_{n1}\cos(\alpha_1) - F_{t1}\sin(\alpha_1) - C_{b1}(\dot{x}_{i1} - \dot{x}_{o1}) - K_{b1}(x_{i1} - x_{o1}),$$

$$M_{i1}\ddot{y}_{i1} = F_{n1}\sin(\alpha_1) + F_{t1}\cos(\alpha_1) - C_{b1}(\dot{y}_{i1} - \dot{y}_{o1}) - K_{b1}(y_{i1} - y_{o1}),$$

$$M_{o1}\ddot{x}_{o1} = C_{b1}(\dot{x}_{i1} - \dot{x}_{o1}) + K_{b1}(x_{i1} - x_{o1}) - K_{s1}x_{o1} - C_{s1}\dot{x}_{o1},$$

$$M_{o1}\ddot{y}_{o1} = C_{b1}(\dot{y}_{i1} - \dot{y}_{o1}) + K_{b1}(y_{i1} - y_{o1}) - K_{s1}y_{o1} - C_{s1}\dot{y}_{o1},$$

$$I_{pb}\ddot{\theta}_{i1} = F_{t1}R_b - T_{d1}.$$

The EOMs for the bottom CB are

$$M_{i2}\ddot{x}_{i2} = F_{n2}\cos(\alpha_2) - F_{t2}\sin(\alpha_2) - C_{b2}(\dot{x}_{i2} - \dot{x}_{o2}) - K_{b2}(x_{i2} - x_{o2}),$$

$$M_{i2}\ddot{y}_{i2} = F_{n2}\sin(\alpha_2) + F_{t2}\cos(\alpha_2) - C_{b2}(\dot{y}_{i2} - \dot{y}_{o2}) - K_{b2}(y_{i2} - y_{o2}),$$

$$M_{o2}\ddot{x}_{o2} = C_{b2}(\dot{x}_{i2} - \dot{x}_{o2}) + K_{b2}(x_{i2} - x_{o2}) - K_{s2}x_{o2} - C_{s2}\dot{x}_{o2},$$

$$M_{o2}\ddot{y}_{o2} = C_{b2}(\dot{y}_{i2} - \dot{y}_{o2}) + K_{b2}(y_{i2} - y_{o2}) - K_{s2}y_{o2} - C_{s2}\dot{y}_{o2},$$

$$I_{pb}\ddot{\theta}_{i2} = F_{t2}R_b - T_{d2} + T_{za},$$

where $C_{b1,2}$ and $K_{b1,2}$ are the CB damping and stiffness, $C_{s1,2}$ and $K_{s1,2}$ are the support damping and stiffness, and R_b is the bore radius of the CB. The parameter $K_{b1,2}$ is calculated according to the axial preload and inner race speed.

From Fig. 3, the axial model is developed as

$$M_m\ddot{z}_m = -K_{ma}(z_m - z_r) - C_{ma}(\dot{z}_m - \dot{z}_r) + M_m g,$$

$$M_f\ddot{z}_f = -K_{fa}(z_f - z_r) - C_{fa}(\dot{z}_f - \dot{z}_r) + M_f g,$$

$$M_r\ddot{z}_r = K_{ma}(z_m - z_r) + C_{ma}(\dot{z}_m - \dot{z}_r) + K_{fa}(z_f - z_r) + C_{fa}(\dot{z}_f - \dot{z}_r) - F_{cz} + M_r g,$$

$$M_i\ddot{z}_i = -K_{ba}(z_i - z_o) - C_{ba}(\dot{z}_i - \dot{z}_o) + F_{cz},$$

$$M_o\ddot{z}_o = K_{ba}(z_i - z_o) + C_{ba}(\dot{z}_i - \dot{z}_o) - K_{sa}z_o - C_{sa}\dot{z}_o,$$

where K_{ba} is the axial stiffness of the bottom CB, which is also calculated from the axial preload and inner race speed.

Appendix B. Nomenclature

C	damping
F	contact force
I	moment of inertia

K	stiffness
M	mass
e	unbalance eccentricity
α	contact angle

Subscripts

a	axial
b	bearing
d	drag
f	flywheel
i	inner race
m	motor
n	normal
o	outer race
p	polar
r	rotor or rotational
s	support system
t	transverse or tangential
1 and 2	top and bottom

References

[1] A. Gelin, J.M. Pugnet, J. Der Hagopian, Dynamic behavior of flexible rotors with active magnetic bearings on safety auxiliary bearings, Proceedings of Third International Conference on Rotordynamics, Lyon, France, 1990, pp. 503–508.

[2] T. Ishii, R.G. Kirk, Transient response technique applied to active magnetic bearing machinery during rotor drop, American Society of Mechanical Engineers, Journal of Rotating Machinery and Vehicle Dynamics 35 (1991) 191–199.

[3] R.G. Kirk, T. Ishii, Transient rotor drop analysis of rotors following magnetic bearing power outage, Proceedings of MAG '93 Magnetic Bearings, Magnetic Drives, and Dry Gas Seals Conference & Exhibition, Alexandria, VA, USA, 1993, pp. 53–61.

[4] M. Fumagalli, P. Varadi, G. Schweitzer, Impact dynamics of high speed rotors in retainer bearings and measurement concepts, Proceedings of the Fourth International Symposium on Magnetic Bearings, Zurich, Switzerland, 1994, pp. 239–244.

[5] W.C. Foiles, P.E. Allaire, Nonlinear transient modeling of active magnetic bearing rotors during rotor drop on auxiliary bearings, Proceedings of MAG '97 Industrial Conference and Exhibition on Magnetic Bearings, Alexandria, VA, USA, 1997, pp. 154–163.

[6] R. Gorden Kirk, et al., Rotor drop test stand for AMB rotating machinery. Part I: description of test stand and initial results, Proceedings of the Fourth International Symposium on Magnetic Bearings, Zurich, Switzerland, 1994, pp. 207–212.

[7] R. Gordon Kirk, et al., Rotor drop test stand for AMB rotating machinery. Part II: steady state analysis and comparison to experimental results, Proceedings of the Fourth International Symposium on Magnetic Bearings, 1994, pp. 213–218.

[8] E.E. Swanson, R.G. Kirk, J. Wang, AMB rotor drop initial transient on ball and solid bearings, Proceedings of MAG '95 Magnetic Bearings, Magnetic Drive and Dry Gas Seals Conference & Exhibition, Alexandria, VA, USA, 1995, pp. 207–216.

[9] L.P. Tessier, The development of an auxiliary bearing landing system for a flexible AMB-supported hydrogen process compressor rotor, Proceedings of MAG '97 Industrial Conference and Exhibition on Magnetic Bearings, Alexandria, VA, USA, 1997, pp. 120–128.
[10] H.M. Chen, et al., Test of zero clearance auxiliary bearing, Proceedings of MAG '97 Industrial Conference and Exhibition on Magnetic Bearings, Alexandria, VA, USA, 1997, pp. 111–119.
[11] Huajun Xie, G.T. Flowers, Steady-state dynamic behavior of an auxiliary bearing supported rotor system, American Society of Mechanical Engineers Winter Annual Meeting, Chicago, November 1994, pp. 1–11.
[12] H. Ecker, Steady-state orbits of an AMB-supported rigid rotor contacting the backup bearings, Proceedings of MAG '97 Industrial Conference and Exhibition on Magnetic Bearings, Alexandria, VA, USA, 1997, pp. 129–138.
[13] B.F. Feeny, Stability of cylindrical and conical motions of a rigid rotor in retainer bearings, Proceedings of the Fourth International Symposium on Magnetic Bearings, Zurich, Switzerland, 1994, pp. 219–224.
[14] E.H. Maslen, L.E. Barrett, Feasible whirl of rotors in auxiliary bearings, Proceedings of MAG '95: Magnetic Bearings, Magnetic Drives and Dry Gas Seals, Alexandria, VA, USA, 1995, pp. 217–226.
[15] J.M. de Mul, et al., Equilibrium and associated load distribution in ball and roller bearings loaded in five degrees of freedom while neglecting friction—Part I: general theory and application to ball bearings, Transactions of American Society of Mechanical Engineers, Journal of Tribology 111 (1989) 142–148.
[16] Y.C. Shin, Bearing nonlinearity and stability analysis in high speed machining, Transactions of American Society of Mechanical Engineers, Journal of Engineering for Industry 114 (1992) 23–30.
[17] B.R. Jorgensen, Y.C. Shin, Dynamics of machine tool spindle/bearing systems under thermal growth, Transactions of American Society of Mechanical Engineers, Journal of Tribology 119 (1997) 875–882.
[18] T.A. Harris, Rolling Bearing Analysis, 2nd Edition, Wiley-Interscience Publication, New York, 1984.
[19] S.P. Timoshenko, J.N. Goodier, Theory of Elasticity, 3rd Edition, McGraw-Hill International Editions, Singapore, 1970.
[20] Crawford Meeks, User Manual for BASDREL Computer Program, Crawford & Associates, Calabasas, 2000.